

AD-A093 736

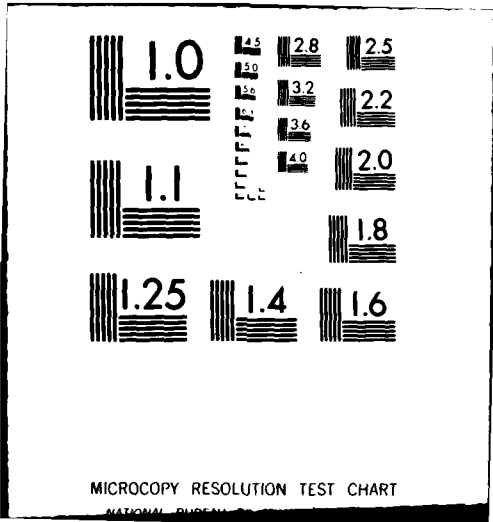
SCIENTIFIC RESEARCH ASSOCIATES INC GLASTONBURY CT F/G 20/4
COMPUTATION OF LAMINAR AND TURBULENT FLOW IN CURVED DUCTS; CHAN--ETC(U)
DEC 80 R C BUEGELN, W R BRILEY, H MCDONALD N00014-79-C-0713
SRA-R80-920006-F NL

UNCLASSIFIED

For I
6/1/79



END
DATE
FILMED
2 -81
DTIC



MICROCOPY RESOLUTION TEST CHART

NATIONAL BUREAU OF STANDARDS-1963-A

R80-920006-F

12

LEVEL II

ANALYSIS OF LAMINAR AND TURBULENT FLOW IN CURVED DUCTS,
CHANNELS, AND PIPES USING THE NAVIER-STOKES EQUATIONS

C. Buggeln, W. R. Briley, and H. McDonald
Scientific Research Associates, Inc.
P.O. Box 498
Westonbury, CT 06033

DTIC
SELECTED
S JAN 13 1981 D
E

December 1980

Final Report for Period 1 October 1979 - 30 September 1980

Approved for Public Release; Distribution Unlimited

Prepared for

OFFICE OF NAVAL RESEARCH
400 N. Quincy Street
Arlington, VA 22217

81 1 12 068

AD A0893738

14
SRA

REPORT DOCUMENTATION PAGE

READ INSTRUCTIONS BEFORE COMPLETING FORM

1. REPORT NUMBER - R80-920006-F
 2. GOVT ACCESSION NO. AD A093736
 3. RECIPIENT'S CATALOG NUMBER

6

4. TITLE (and Subtitle)
 Computation of Laminar and Turbulent Flow in Curved Ducts, Channels and Pipes Using the Navier-Stokes Equations.

9

5. TYPE OF REPORT & PERIOD COVERED
 Final Report. 1 Oct 79-30 Sep 80
 79 Oct. 1 to 80 Sept. 30

10

6. AUTHOR(s)
 R. C./Buggeln, W. R./Briley, H./McDonald

15

7. CONTRACT OR GRANT NUMBER(s)
 N00014-79-C-0713

8. PERFORMING ORGANIZATION NAME AND ADDRESS
 Scientific Research Associates, Inc.
 P.O. Box 498
 Glastonbury, CT 06033

10. PROGRAM ELEMENT, PROJECT, TASK AREA & WORK UNIT NUMBERS

11. CONTROLLING OFFICE NAME AND ADDRESS
 Office of Naval Research
 800 N. Quincy Street
 Arlington, VA 22217

11

12. REPORT DATE
 December 1980
 13. NUMBER OF PAGES

14. MONITORING AGENCY NAME & ADDRESS (if different from Controlling Office)
 12 42

15. SECURITY CLASS. (of this report)
 Unclassified
 15a. DECLASSIFICATION/DOWNGRADING SCHEDULE

16. DISTRIBUTION STATEMENT (of this Report)
 Approved for Public Release; Distribution Unlimited

17. DISTRIBUTION STATEMENT (of the abstract entered in Block 20, if different from Report)

18. SUPPLEMENTARY NOTES

19. KEY WORDS (Continue on reverse side if necessary and identify by block number)
 Three-Dimensional Flow
 Curved Ducts and Pipes
 Navier-Stokes Equations
 Turbulent Flow

20. ABSTRACT (Continue on reverse side if necessary and identify by block number)
 Both laminar and turbulent flows in strongly curved ducts, channels, and pipes are studied by numerical methods. The study concentrates on the curved square-duct geometry and flow conditions for which detailed measurements have been obtained recently by Taylor, Whitelaw, and Yianneskis. The solution methodology encompasses solution of the compressible ensemble-averaged Navier-Stokes equations at low Mach number using a split linearized block implicit (LBI) scheme, and rapid convergence on the order of 80 noniterative

time steps is obtained. The treatment of turbulent flows includes resolution of the viscous sublayer region. A series of solutions for both laminar and turbulent flow and for both two- and three-dimensional geometries of the same curvature are presented. The accuracy of these solutions is explored by mesh refinement and by comparison with experiment. In summary, good qualitative and reasonable quantitative agreement between solution and experiment is obtained. Collectively, this sequence of results serves to clarify the physical structure of these flows and hence how grid selection procedures might be adjusted to improve the numerical accuracy and experimental agreement. For a three-dimensional flow of considerable complexity, the relatively good agreement with experiment obtained for the turbulent flow case despite a coarse grid must be regarded as encouraging.

TABLE OF CONTENTS

	Page
INTRODUCTION.	1
Previous Work.	2
THE PRESENT APPROACH.	4
Coordinate System.	5
Boundary and Initial Conditions.	5
Governing Equations and Differencing Procedures.	7
Split LBI Algorithm.	8
COMPUTED RESULTS.	10
Mesh Refinement and Other Validation Tests	10
Three-Dimensional Curved Duct and Pipe Flows	12
SUMMARY AND CONCLUSIONS	15
REFERENCES.	16
FIGURES	18

Accession For	
NTIS GRA&I	<input checked="" type="checkbox"/>
DTIC TAB	<input type="checkbox"/>
Unannounced	<input type="checkbox"/>
Justification	
By _____	
Distribution/ _____	
Availability Codes	
Dist	Avail and/or Special
A	

INTRODUCTION

The present study considers both laminar and turbulent flow in curved ducts, pipes, and channels of constant cross sectional area and shape. The particular flows considered here, as well as similar flows in related geometries, are very common in internal flow applications. They are of interest in connection with flow degradation and their strong influence on flow losses and heat transfer levels.

The general character of flow in curved ducts and pipes is known to differ fundamentally from that in straight flow geometries, due to the presence of large secondary flows which distort the primary flow. Since strong deflections may occur over a short distance, such flows are usually of a transition type and seldom become fully developed or assume any convenient similarity form. By analogy with external flows, the flow often behaves as an inviscid flow in a central core region, with viscous effects limited to regions near solid boundaries. Unlike most external flow problems, however, the inviscid core region is often not an irrotational potential flow but is rotational with interaction between the viscous and rotational inviscid flow regions. Furthermore, as the flow passes through successive flow passages, new viscous and thermal boundary layers develop beneath previous boundary layers, and the distinction between rotational inviscid and viscous boundary layer regions can become tenuous.

The underlying physical mechanisms present in flows of this type are clearly elucidated by secondary flow theory (reviewed for example by Horlock & Lakshminarayana [1]). In its most common and perhaps simplest form, the secondary flow is generated by turning a primary flow in which viscous or other forces upstream have produced a non-zero velocity gradient normal to the plane of curvature. Fluid with above (/below) average momentum migrates to the outside (/inside) of the bend as a result of the radial pressure gradients produced by turning the flow. This phenomenon is quantified by secondary flow theory as the generation of streamwise vorticity from transverse vorticity which has been produced upstream. Although the secondary flow is generated by an inviscid mechanism, its strength and subsequent development are influenced in varying degrees by viscous effects. In any event, the secondary flows are often quite large and the flow patterns are thus complex and highly three-dimensional. Two-dimensional flows in curved channels do not behave in this manner (provided the flow remains two-dimensional), since there can be no streamwise vorticity component in a two-dimensional flow.

Previous Work

Much of the early work on flow in curved ducts and pipe bends can be traced from the reviews of Hawthorne [2, 3]. Of primary interest here are methods for computing such flows and experimental work which may be useful in evaluating the numerical predictions. Only three-dimensional developing flows in curved ducts and pipe bends are considered. Two-dimensional flows and flows which are fully developed and thus do not vary with an axial coordinate are excluded from consideration.

Flow in Curved Ducts

Pratap and Spalding [4] have considered turbulent flow in a strongly curved duct using their "partially parabolic" calculation procedure and a two-equation/wall-function turbulence model. Ghia and Sokhey [5] have computed laminar flow in ducts of strong curvature using a parabolized form of the Navier-Stokes equations. Kreskovsky, Briley, and McDonald [6] have recently applied an approximate initial-value analysis for viscous primary and secondary flows to laminar and turbulent flow in strongly curved ducts, using a one-equation turbulence model with viscous sublayer resolution. Humphrey, Taylor and Whitelaw [7] have obtained laser-Doppler anemometry measurements of laminar flow in a square duct of strong curvature, for the case of fully developed flow in the straight section upstream of the bend. For comparison, then also performed numerical calculations for this flow using a version of the fully-elliptic calculation procedure developed at Imperial College by Gosman, Pun, Patankar and Spalding. Further extensive calculations including heat transfer effects have been made recently by Yee and Humphrey [8]. Finally, Taylor, Whitelaw and Yianneskis [9] have recently made extensive measurements of both laminar and turbulent flow in a strongly curved square duct with moderately thin boundary layers at the entrance to the bend. The present study concentrates heavily on numerical solutions of the Navier-Stokes equations for the flow conditions of these measurements of Taylor, Whitelaw and Yianneskis.

Flow in Pipe Bends

Rowe [10] has taken total pressure measurements for turbulent flow in a pipe bend of small curvature. For comparison, he also performed flow calculations based on the Squire-Winter inviscid secondary-flow approximation. Patankar, Pratap and Spalding [11, 12] have performed calculations for both laminar and turbulent flow in pipe bends of small curvature, using their "parabolic flow" calculation procedure and a two-equation/wall-function turbulence model. Agrawal, Talbot and Gong [13]

have obtained detailed measurements of laminar flow development in curved pipes with uniform velocity at entry. These measurements would be useful for evaluation of numerical computations.

THE PRESENT APPROACH

The present objective is to explore and evaluate a method for predicting turbulent flows in ducts and pipes of strong curvature by numerical solution of the Navier-Stokes equations. A time-dependent formulation is used as an iterative means of obtaining steady solutions, and the compressible form of the equations are solved in the low Mach number regime ($M \pm 0.05$), which closely approximates an incompressible flow. The governing equations are solved using a consistently-split linearized block implicit (LBI) scheme developed by Briley and McDonald [14, 15]. With proper treatment of boundary conditions, this algorithm provides rapid convergence which is not significantly degraded by the extreme local mesh resolution which is necessary for the near-wall sublayer region in turbulent flows. The turbulence model used is a one-equation model recently explored by Shamroth and Gibeling [15]. This model requires solution of a single equation governing turbulence kinetic energy q^2 , in conjunction with an algebraically specified length scale. The turbulent effective viscosity μ_t is obtained from the Prandtl-Kolomogorov constitutive relationship $\mu_t = \ell(q^2)^{1/2}$. The model also includes representation of the influence of turbulence Reynolds number on turbulent stress levels and provides for resolution of the near-wall viscous sublayer region.

The present effort concentrates on the geometry and flow conditions for which detailed measurements have been obtained recently by Taylor, Whitelaw, and Yianneskis [9]. This geometry is shown to scale in Fig. 1 and consists of a square duct with a 90 degree circular arc bend and with straight sections both upstream and downstream of the bend. The ratio of bend radius R to duct width W is 2.3. The measurements were taken for Reynolds numbers based on mean velocity and duct width of 790 (laminar flow) and 40,000 (turbulent flow). In each case, moderately thin shear layers (20 - 30% of duct width) were present at the start of the bend. The present study considers both of these measured flows and in addition the corresponding two-dimensional channel flows having the same Reynolds numbers, shear layer thickness and ratio of bend radius to duct width. The two-dimensional channel flows are computed to establish their flow structure for comparison with the three-dimensional duct flow solutions. Test calculations are performed to establish grid independence and to verify the treatment of inflow/outflow conditions for the two-dimensional channel flows. The laminar and turbulent duct flow solutions are compared with the flow measurements and with the channel flow results to provide an evaluation of the flow predictions obtained by the present computational procedure. Finally, turbulent flow in a curved pipe with radius ratio of 24 and Reynolds number of 2.36×10^5 is computed and compared with the measurements of Rowe [10].

Coordinate System

The compressible Navier-Stokes equations in general orthogonal coordinates are solved using analytical coordinate data for a system of coordinates aligned with the duct geometry. The coordinate system is shown in Fig. 2 and consists of an axial coordinate x_1 parallel to a curved duct centerline (which lies in the Cartesian x - y plane), and general orthogonal coordinates x_2 , x_3 in transverse planes normal to the centerline. If the axial coordinate x_1 denotes distance along the centerline and if $K(x_1) \equiv 1/R(x_1)$ is the centerline curvature, then the metric scale factor h_1 for the axial coordinate direction is given by $h_1 = 1 + K(x_1) \Delta R(x_2, x_3)$, where $\Delta R \equiv r - R$ is independent of x_1 . The transverse metric factors are given by $h_2 = h_3 = 1$ for rectangular (Cartesian) cross sections and by $h_2 = 1$, $h_3 = x_2$ for circular (polar) cross sections. The quantity ΔR is given by $\Delta R = x_3$ and $\Delta R = x_2 \cos x_3$ for Cartesian and polar cross sections, respectively. The centerline curvature K is discontinuous when a straight segment of a duct joins a constant radius segment. To remove the associated coordinate singularity, the flow geometry is smoothed over an axial distance of one duct diameter. This is accomplished using a cubic polynomial variation in K which matches both function value and slope of K at the end points of the smoothing region.

Boundary and Initial Conditions

The computational domain is chosen to be a region in the immediate vicinity of the duct bend (cf. Fig. 1) embedded within a larger overall flow system upstream and downstream of the bend. This choice of computational domain requires inflow and outflow boundary conditions which adequately model the interface between the computed flow and the remainder of the flow system. The inflow/outflow conditions used are derived from an assumed flow structure and are chosen to provide:

- (a) inflow with prescribed stagnation pressure and temperature in an inviscid core region, and with a given axial velocity profile shape in shear layers, and
- (b) outflow with a prescribed static pressure distribution.

These boundary conditions are chosen following consideration both of a one-dimensional inviscid characteristics analysis and of the physical process by which many duct flows are established. For subsonic flow, a characteristics analysis of the one-dimensional inviscid Euler equations indicates that two boundary conditions are required at an

inflow boundary and one additional boundary condition is required at outflow. Physically, a duct flow is often established by supplying air of a given stagnation pressure and temperature and exhausting the duct at a given static pressure. The mass flux through the duct may then vary with time until a steady state is achieved, at which the mass flux is determined as a balance between these inflow/outflow quantities and viscous and thermal effects within the duct. By choosing stagnation pressure and temperature at inflow and static pressure at outflow as the dominant boundary conditions, the present solution procedure allows both velocity and density to vary with time, as is consistent with this physical process. As a consequence, pressure waves can be transmitted through the inflow boundary during the transient flow process and are not reflected back into the computational domain. The reflection of pressure waves at an inflow boundary where velocity and density are fixed in time has often been cited as a cause of either instability or slow convergence in other investigations. The specific treatment of initial and boundary conditions used here is outlined below.

The initial and boundary conditions are devised from estimates of the potential flow velocity $\bar{U}_I(x_1, x_2, x_3)$ for the duct, a mean boundary layer thickness $\delta(x_1)$ for shear layers on transverse duct walls, and finally from an estimate of the blockage correction factor $B(x_1)$ for the core flow velocity due to the boundary layer growth. The potential flow velocity is approximated as uniform flow in straight segments of the duct and as proportional to r^{-1} in curved segments. The constants $(R_o - R_i) / \ln(R_o / R_i)$ and $R_o^2 / 2 (R - R_o^2 - R_i^2)$ lead to a unit mass flux for rectangular and circular cross sections, respectively. Here, R_i and R_o are the radii to the inner and outer walls of the duct, and $R = (R_i + R_o) / 2$ as in Fig. 1. Distributions of $\delta(x_1)$ and $B(x_1)$ are determined by recourse to a simple one-dimensional momentum integral analysis using a fixed velocity profile shape and an approximate relationship between B and mean displacement thickness $\delta^*(x_1)$. Details of this procedure are not important, as the results serve mainly as a convenient method of setting approximate initial conditions. Finally, a shear layer velocity profile shape $f(\bar{y}/\delta)$, $0 \leq f \leq 1$ is chosen for each problem, where \bar{y} is a parameter indicative of distance from a wall. The initial values of velocity components u_1, u_2, u_3 are given by

$$u_1 = \bar{U}_I B(x_1) f[\bar{y}/\delta(x)] \quad u_2 = u_3 = 0 \quad (1)$$

A reasonably accurate estimate for the pressure drop which will produce the desired flow rate must be made using any convenient source, such as a Moody diagram, data correlations, momentum integral analysis, or other computed results. A smooth axial distribution of pressure which matches this pressure drop is then assigned and adjusted to approximate local curvature of the flow geometry. This completes specification of the initial conditions. It is noted that although these initial conditions do take into account several relevant features of the flow, the important effects of strong secondary flows and their distortion of the primary flow are completely neglected. The resulting initial flow is thus a simple but relatively crude approximation to the final flow field.

At the inflow boundary, a "two-layer" boundary condition is devised such that stagnation pressure p_0 is fixed in the core flow region and an axial velocity profile shape $u_1/u_e = f(\bar{y}/\delta)$ is set within shear layers. Here, u_e is the local edge velocity which varies with time and is adjusted after each time step to the value consistent with p_0 and the local edge static pressure determined as part of the solution. The remaining inflow conditions are $\partial^2 u_2/\partial n^2 = \partial^2 u_3/\partial n^2 = 0$ and $\partial^2 c_p/\partial n^2 = g(x_2, x_3)$, where n denotes the normal coordinate direction and c_p is pressure coefficient. The quantity g is computed from the initial conditions with c_p defined as $1-(BU_1)^2$, its value from the potential flow corrected for estimated blockage. For outflow conditions, the static pressure is imposed, and second normal derivatives of each velocity component are set to zero. At no-slip walls, all velocity components are set to zero, and the remaining condition used is $\partial p/\partial n = 0$, where p is pressure. The condition $\partial p/\partial n = 0$ at a no-slip surface approximates the normal momentum equation to order Re^{-1} for viscous flow at high Reynolds number. Finally, the three-dimensional flow cases are assumed to be symmetric about the plane containing the curved duct centerline, and symmetry conditions are imposed on this boundary.

Governing Equations and Differencing Procedures

The differencing procedures used are a straightforward adaptation of those used by Briley and McDonald [14] in Cartesian coordinates for flow in a straight duct. The compressible time-dependent Navier-Stokes equations are written in orthogonal coordinates in the form given by Hughes and Gaylord [17]. The first-derivative flux terms are written in conservation form, and for economy the stagnation enthalpy is assumed constant. The definition of stagnation enthalpy and the equation of state for a perfect gas can then be used to eliminate pressure and temperature as dependent variables, and solution of the energy equation is unnecessary. The continuity and

three momentum equations are solved with density and the three velocity components aligned with the coordinates as dependent variables. Three-point central differences were used for spatial derivatives, and second-order artificial dissipation terms are added as in [14] to prevent spatial oscillations at high cell Reynolds number. This treatment lowers the formal accuracy to first order but does not seriously degrade accuracy in representing viscous terms in thin shear layers. Analytical coordinate transformations due to Roberts [18] were used to redistribute grid points and thus improve resolution in shear layers. Derivatives of geometric data were determined analytically for use in the difference equations.

The turbulence model used is a one-equation model recently explored by Shamroth and Gibeling [15]. This model requires solution of a single equation governing turbulence kinetic energy q^2 , in conjunction with an algebraically specified length scale ℓ . The equation governing the balance of turbulence kinetic energy, q^2 , in curvilinear orthogonal coordinates was derived from the Cartesian tensor form of this equation given by Launder and Spalding [19]. For the present application, a very simple three-layer length scale was constructed with the outer or wake scale determined by a one-dimensional estimate of the growth of this wake length scale from its value on inlet. This growth rate was essentially obtained from the Von Karman momentum integral equation assuming the wake length scale would grow roughly as the boundary layer thickness. Near the nearest wall the length scale was assumed to vary in accordance with Von Karman's linear relationship $\ell=ky$. In the viscous sublayer the length scale was damped by viscous effects according to Van Driest's formulation. Finally, the turbulent effective viscosity μ_t was obtained from the Prandtl-Kolomogorov constitutive relationship $\mu_t \propto \ell(q^2)^{1/2}$. The turbulent viscosity was then supposed isotropic and the stress tensor in the ensemble averaged equations determined by adding the turbulent viscosity to the kinetic viscosity. The turbulent kinetic energy near the wall was damped out according to the suggestion of Shamroth and Gibeling (Ref. 15).

Split LBI Algorithm

The numerical algorithm used is the consistently-split "linearized block implicit" (LBI) scheme developed by Briley and McDonald [14, 15] for systematic use in solving systems of nonlinear parabolic-hyperbolic partial differential equations (PDE's). To illustrate the algorithm, let

$$(\phi^{n+1} - \phi^n) / \Delta t = \beta D(\phi^{n+1}) + (1-\beta) D(\phi^n) \quad (2)$$

approximate a system of time-dependent nonlinear PDE's (centered about $t^n + \beta \Delta t$) for the vector ϕ of dependent variables, where D is a multidimensional vector spatial differential operator, and t is a discretized time variable such that $\Delta t = t^{n+1} - t^n$. A local time linearization (Taylor expansion about ϕ^n) is introduced, and this serves to define a linear differential operator L such that

$$D(\phi^{n+1}) = D(\phi^n) + L^n(\phi^{n+1} - \phi^n) + O(\Delta t^2) \quad (3)$$

Eq. (2) can thus be written as the linear system

$$(I - \beta \Delta t L^n)(\phi^{n+1} - \phi^n) = \Delta t D(\phi^n) \quad (4)$$

without lowering the formal accuracy.

The multidimensional operator L is divided into three "one-dimensional" sub-operators $L = L_1 + L_2 + L_3$ (associated here with the three coordinate directions), and Eq. (4) is split as in the scalar development of Douglas & Gunn [20] and is written as

$$(I - \beta \Delta t L_1^n)(\phi^* - \phi^n) = \Delta t D(\phi^n) \quad (5a)$$

$$(I - \beta \Delta t L_2^n)(\phi^{**} - \phi^n) = \phi^* - \phi^n \quad (5b)$$

$$(I - \beta \Delta t L_3^n)(\phi^{***} - \phi^n) = \phi^{**} - \phi^n \quad (5c)$$

$$\phi^{n+1} = \phi^{***} + O(\Delta t^3) \quad (5d)$$

If spatial derivatives appearing in L are replaced by three-point difference formulas, then each step in Eqs. (5a-c) can be solved by a block-tridiagonal "inversion". Eliminating the intermediate steps in Eqs. (5a-d) results in

$$(I - \beta \Delta t L_1^n)(I - \beta \Delta t L_2^n)(I - \beta \Delta t L_3^n)(\phi^{n+1} - \phi^n) = \Delta t D(\phi^n) \quad (6)$$

which approximates Eq. (4) to order Δt^3 . Complete derivations are given by the authors in [14, 15]. It is noted that Warming and Beam [21] have suggested an alternate derivation for this and other related algorithms, based on the approximate factorization approach of Yanenko and D'Yakonov [22]. Their derivation is equivalent up to Eq. (4) and proceeds immediately to Eq. (6) by observing that Eq. (6) is a "delta form" approximate factorization of Eq. (4). Eq. (6) is then solved by introducing intermediate quantities $(\phi^* - \phi^n)$ and solving Eqs. (5a-c).

COMPUTED RESULTS

Extensive calculations were made for the flow geometry in which detailed measurements were obtained by Taylor, Whitelaw, and Yianneskis [9]. This geometry is shown in Fig. 1 and consists of a square duct with a 90 degree circular-arc-bend and with straight sections both upstream and downstream of the bend. The ratio of bend radius to duct width is 2.3. The measurements were taken for Reynolds numbers based on mean velocity and duct width of 790 (laminar flow) and 40,000 (turbulent flow). In each case, moderately thin shear layers (20-30% of duct width) were present at the start of the bend. Both of these measured flows were computed. In addition the corresponding two-dimensional channel flows having the same curvature, Reynolds number and shear layer thickness were computed for comparison with the three-dimensional duct flow solutions.

Mesh Refinement and Other Validation Tests

Test calculations were first performed for the two-dimensional channel flows to establish grid independence and to verify the treatment of inflow/outflow conditions. The results are shown in Figs. 3-5. In Fig. 3, axial velocity profiles at the 60° location are shown for both laminar and turbulent flow and for three radial grid densities. With the 26 x 28 grid, the mesh spacing (in channel widths) adjacent to the wall is 0.0026 (turbulent) and 0.0087 (laminar). The results in Fig. 3 indicate that 26 radial grid points are sufficient to resolve this flow. In Fig. 4, the wall pressure coefficient c_p is shown for both laminar and turbulent flow and for two axial grid densities. Here and elsewhere in this report, the axial coordinate is given in degrees of turning within the bend and in duct widths upstream or downstream of the bend. The results in Fig. 4 are not sensitive to the axial grid used. Note that at the inflow boundary, a transverse pressure gradient is permitted by the imposed inflow boundary conditions and does occur in Fig. 4. The static pressure is assumed constant at the downstream outflow boundary. In Fig. 5, the effect of extending the straight segments to a length of 3.5 channel widths both upstream and downstream of the bend is shown. Although the extensions had no observable effect on the turbulent flow results, there is a noticeable effect near the 90° location for the laminar flow. This sensitivity of the laminar flow can be explained by the occurrence of a very small flow separation on the inner wall in this region. Evidently, although the solutions are insensitive to the axial grid, the downstream boundary is apparently

located too close to this flow separation unless extensions are added. This flow separation did not occur in the three-dimensional square duct analog of this flow, however, and the extensions were not included in these latter calculations.

On balance, it is concluded that a 26 x 28 grid, distributed to provide local resolution for the near-wall region, was sufficient to achieve grid independence for the two-dimensional channel cases. This same grid was used for the three-dimensional duct calculations, and the mesh distribution for the third coordinate was chosen with the two-dimensional results as a guide. Taking advantage of symmetry about the plane midway between the endwalls, a 26 x 28 x 13 grid was used, with mesh spacing adjacent to the endwall of 0.0028 (turbulent) and 0.0091 (laminar) duct widths. Since the two- and three-dimensional flows have a different structure, the resulting grid does not guarantee accuracy in three dimensions. Nevertheless, knowledge of the two-dimensional accuracy is very useful in evaluating the three-dimensional results, for which extensive mesh refinement results were not feasible.

Finally, it is necessary to establish and document both the degree and rate of convergence obtained in the computed solutions. The behavior of maximum change in computed streamwise velocity with nondimensional time is shown in Fig. 6 for the two-dimensional turbulent channel flow. These results are typical of those obtained in both two- and three-dimensions and for both laminar and turbulent flow. Also shown in Fig. 6 is the time step number. Here, the particle residence time of 6.75 represents the nondimensional time required for a particle travelling with the reference (mean) velocity to traverse the duct centerline (6.75 duct widths) from inflow to outflow. In this calculation, the initial time step was increased gradually from 0.02 to 0.5 in the first 15 steps, held constant at 0.5 for the next 15 steps, and thereafter a sequence of 5 time steps in equal logarithmic increments between 0.01 and 0.5 was used cyclically. The normalized maximum increment in velocity shown in Fig. 6 is shown only for the maximum time step of 0.5. It should be emphasized that Fig. 6 would not be meaningful if the increment were not taken at a large time step, since the temporal increment can be made arbitrarily small by taking a small time step. With 10^{-4} as the criterion, convergence to the steady state was usually obtained at around 80 time steps in both two- and three-dimensional flow. Residuals in the governing equations were also examined at convergence and noted to be small in comparison to the other terms in the governing equations. As a final observation, with 10^{-4} as the criterion, the plotted results exhibited little or no discernable change with further iteration. The behavior observed in Fig. 6 does represent rapid convergence for a problem of this complexity, and this is attributed in part to the use of an implicit algorithm (including boundary conditions) and in part to the

selection of inflow/outflow boundary conditions. The specification of total pressure at inflow and static pressure at outflow allows pressure waves to be transmitted through the inflow boundary during the transient process, and this avoids the instability or slow convergence often attributed to reflection of pressure waves and an inflow boundary with fixed velocity and density.

Three-Dimensional Curved Duct and Pipe Flows

Axial velocity profiles for turbulent flow in both the two-dimensional channel and in the symmetry plane $x_3 = 0$ of the three-dimensional duct are shown at selected locations in Fig. 7. Also shown are the duct flow measurements of Taylor, Whitelaw & Yianneskis [9]. The two-dimensional turbulent channel flow was not compared with experimental measurements, although as mentioned they were shown to be essentially grid independent. The computed flow structure for the channel flow consists of an inviscid core flow with acceleration near the inner wall of the bend, and with shear-layer velocity profiles characteristic of turbulent flow. For comparison, also shown in Fig. 7 are velocity profiles in the symmetry plane for the three-dimensional duct flow. Here, there is evidence of considerable flow distortion as a result of secondary flow, which is directed toward the inner wall near the endwalls ($x_3 = +0.5$) and toward the outer wall near the symmetry plane ($x_3 = 0$). Although the axial velocity in the symmetry plane initially accelerates near the inner wall up to the 30° location (duplicating the channel flow behavior), beyond this point the peak velocity shifts toward the outer wall. This pattern is also present in the data of Taylor, Whitelaw and Yianneskis [9], and the level of agreement shown in Fig. 7 is generally good except near the inner wall near the end of the bend. Radial velocity profiles at the 77.5 degree location are shown in Fig. 8 and display a very strong secondary flow near the endwall with peak velocity up to 40% of the mean axial velocity, located very near the endwall surface. Near the symmetry plane, the radial velocity is of order 20% of the mean axial velocity and is directed toward the outer wall. The computed radial velocity is in very good agreement with the measurements except in the region near the symmetry plane and inner wall. On balance, the level of agreement between prediction and experiment is good; the discrepancy may be due to the turbulence model, but other factors such as grid resolution may still be present. In fact, for a three-dimensional sublayer-resolved turbulent flow calculation with relatively coarse grid, the level of agreement is perhaps better than might be anticipated.

To explore further the accuracy of the predictions, laminar flow in the same geometry was also considered. Computed results for laminar axial and radial velocity profiles corresponding to those given for turbulent flow are shown in Figs. 9 and 10. The two-dimensional laminar flow in Fig. 9 resembles the corresponding turbulent flow in that the flow accelerates near the inner wall of the bend. The velocity profiles are characteristic of laminar flow, however, and since the growth rate of laminar shear layers is greater than that of turbulent flow, there is less evidence of an inviscid core region in the downstream profiles. In addition, laminar flow is less resistant to separation in an adverse pressure gradient, and there is a very small flow separation at the inner wall just downstream of the $+0.25$ location (not actually shown in Fig. 9a, but also mentioned earlier in the discussion of Fig. 5). The three-dimensional laminar duct flow profiles in Fig. 9b display even more distortion downstream due to secondary flow than the turbulent case in Fig. 7b. Although very good qualitative agreement with the Taylor, et al measurements is obtained, there is quantitative disagreement, particularly near the 30° location. The radial velocity profiles at $77\text{-}1/2^\circ$ are shown in Fig. 10, and although qualitative agreement is obtained, there is quantitative disagreement similar to that observed in Fig. 8 for turbulent flow but of greater extent. Since the turbulence model has been removed as a factor in the laminar flow calculations, and since there is no reason to suspect the experimental data, the source of disagreement between prediction and experiment is believed to be mesh related. The two-dimensional mesh refinement tests appear to have been inadequate as a guide for the more complicated and extensive three-dimensional flow structure.

One additional set of experimental comparisons shown in Figs. 11 and 12 provides further clarification of these flow predictions. These two figures show the axial development along the duct centerline of the axial and radial velocity components for each of the four solutions (2D/3D and laminar/turbulent). In each of the two-dimensional channel flows, the axial velocity (Fig. 11) undergoes a mild streamwise acceleration due mainly to blockage caused by shear layer growth, and this acceleration is larger in the laminar flow because of the higher growth rate of laminar flow at these respective Reynolds numbers. In the three-dimensional duct flows, the initial (inlet) velocity is higher than the corresponding channel flow because the endwall shear layers of the duct flow (not present in the channel flow) require higher blockage to give the same mean flowrate. The subsequent downstream decreases in axial velocity for the duct flows are a direct consequence of the radial secondary flow, which convects low velocity fluid toward the centerline. This same behavior is also present in the experimental measurements, although the distortion due to

secondary flow is less severe in the calculation than that observed experimentally. In Fig. 12, the corresponding radial velocities are shown with a sign convention such that negative velocity denotes flow toward the inner wall of the bend. In the two-dimensional channel geometry, the behavior is very similar for both laminar and turbulent flow. There is radial flow toward the inner wall near the start of the bend (0°) and toward the outer wall near the bend exit (90°). In the three-dimensional duct geometry, the flow is primarily radially outward within the bend, and the radial flow is significantly stronger in the laminar case, as is consistent with the development of the axial velocity in Fig. 11. This same flow behavior is evident in the experimental measurements, and although the peak radial velocity is underpredicted in the laminar case, the agreement with experiment is remarkably good in the turbulent case. The stronger secondary flows observed in the laminar case are believed to be the result of the different axial velocity distributions entering the bend. The laminar velocity distribution contains larger transverse (radial) vorticity than the turbulent case except in the viscous dominated region near the walls, and based on secondary flow theory, this should lead to stronger secondary flows. The laminar case thus proved to be a more difficult prediction than the turbulent case.

Finally, total pressure contours computed for turbulent flow in a mildly curved circular pipe are compared with the experimental measurements of Rowe [10] in Fig. 9. Shown are contours of total pressure difference $(p_t - p_r) / \frac{1}{2} \rho_r u_r^2$, where p_t is total pressure and p_r , ρ_r , and u_r are reference values of static pressure, density, and velocity, respectively, taken as their values at the pipe centerline at 0° . The total pressure contours are a sensitive indicator of the distortion which occurs as a result of both viscous losses and secondary flow. In general there is good qualitative agreement between prediction and measurement. Again, the quantitative disagreement which is present is believed to be mesh-related. A $30 \times 19 \times 15$ grid was used for the axial, circumferential and radial directions, respectively. The minimum radial mesh increment at the pipe wall is 0.000765 diameters, and the maximum radial mesh increment at the centerline is 0.12 diameters. This high degree of mesh nonuniformity was needed to provide viscous sublayer resolution at the Reynolds number ($Re_D = 2.36 \times 10^5$) of this case; the use of only 15 radial grid points under these circumstances may be inadequate.

SUMMARY AND CONCLUSIONS

A solution methodology is described for treatment of flow in curved ducts and pipes, and it is demonstrated that rapid convergence (≈ 80 noniterative time-steps) can be obtained for three-dimensional turbulent flows, with sublayer resolution.

A series of solutions for both laminar and turbulent flow and for both two and three-dimensional geometries of the same curvature are presented. The accuracy of these solutions is explored by mesh refinement and by comparison with experiment.

In summary, good qualitative and reasonable quantitative agreement between solution and experiment was obtained. Collectively, this sequence of results serves to clarify the physical structure of these flows and hence how grid selection procedures might be adjusted to improve the numerical accuracy and experimental agreement. For a three-dimensional flow of considerable complexity, the relatively good agreement with experiment obtained for the turbulent flow case despite a coarse grid must be regarded as encouraging. These results seem to warrant further study to clarify the sources of error present and also to perform calculations for additional geometric configurations and flow conditions.

REFERENCES

1. Horlock, J. H. and Lakshminarayana, B.: "Secondary Flows; Theory, Experiment and Application in Turbomachinery Aerodynamics", Annual Rev. Fluid Mech., Vol. 5, 1973, p. 247.
2. Hawthorne, W. R.: "The Applicability of Secondary Flow Analyses to the Solution of Internal Flow Problems", Fluid Mechanics of Internal Flow, ed. G. Sovran, (Elsevier), 1967, p. 263.
3. Hawthorne, W. R.: "Research Frontiers in Fluid Dynamics", eds. R. J. Seeger and G. Temple, (Interscience), 1965, p. 1.
4. Pratap, V. S. and Spalding, D. B.: "Fluid Flow and Heat Transfer in Three-Dimensional Duct Flows", Int. J. Heat & Mass Transfer, Vol. 19, 1976, p. 1183.
5. Ghia, K. N. and Sokhey, J. S.: "Laminar Incompressible Viscous Flow in Curved Ducts of Rectangular Cross-Sections", J. Fluid Engr., Vol. 99, 1977, p. 640.
6. Kreskovsky, J. P., Briley, W. R. and McDonald, H.: "Prediction of Laminar and Turbulent Primary and Secondary Flows in Strongly Curved Ducts", SRA Report R80-900007-12, September, 1980 (to appear as NASA Contractor's Report).
7. Humphrey, J. A. C., Taylor, A. M. K. and Whitelaw, J. H.: "Laminar Flow in a Square Duct of Strong Curvature", J. Fluid Mech., Vol. 83, 1977, p. 509.
8. Yee, G. and Humphrey, J. A. C.: "Developing Laminar Flow and Heat Transfer in Strongly Curved Ducts of Rectangular Cross-Section. ASME Paper 79-WA/HT-15, 1979.
9. Taylor, A. M. K. P., Whitelaw, J. H., and Yianneskis, M.: Measurements of Laminar and Turbulent Flow in a Curved Duct with Thin Inlet Boundary Layers, Imperial College Report FS/80/29, 1980.
10. Rowe, M.: "Measurements and Computations of Flow in Pipes", J. Fluid Mech., Vol. 43, 1970, p. 771.
11. Patankar, S. V., Pratap, V. S. and Spalding, D. B.: "Prediction of Laminar Flow and Heat Transfer in Helically Coiled Pipes. J. of Fluid Mech., Vol. 62, 1974, p. 539.
12. Patankar, S. V., Pratap, V. S. and Spalding, D. B.: "Prediction of Turbulent Flow in Curved Pipes". J. of Fluid Mech., Vol. 67, 1975, p. 583.
13. Agrawal, Y., Talbot, L. and Gong, K.: "Laser Anemometer Study of Flow Development in Curved Circular Pipes". J. Fluid Mech., Vol. 85, 1978, p. 497.
14. Briley, W. R. and McDonald, H.: "Solution of the Multidimensional Compressible Navier-Stokes Equations by a Generalized Implicit Method, J. of Comp. Physics, Vol. 24, Aug. 1977, p. 372.
15. Briley, W. R. and McDonald, H.: "On the Structure and Use of Linearized Block ADI and Related Schemes", J. Comp. Physics, Vol. 34, 1980, p. 54.

16. Shamroth, S. J. and Gibeling, H. J.: "The Prediction of the Turbulent Flow Field About an Isolated Airfoil, AIAA Paper 79-1543, 1979.
17. Hughes and Gaylord: "Basic Equations of Engineering Science". Schaum Publishing Co.
18. Roberts, G. O.: "Computational Meshes for Boundary Layer Problems", Proc. 2nd Int. Conf. Num. Meth. Fluid Dynamics, (Springer-Verlag), 1971, p. 171.
19. Launder, B. E. and Spaulding, D. B.: "The Numerical Computation of Turbulent Flows", Computer Methods in Applied Mechanics and Engineering, Vol. 3, 1974, p. 269.
20. Douglas, J. and Gunn, J. E.: "A General Formulation of Alternating Direction Methods", Numerische Math., Vol. 6, 1964, p. 428.
21. Warming, R. F. and Beam, R. M.: "On the Construction and Application of Implicit Factored Schemes for Conservation Laws", Symposium on Computational Fluid Dynamics, New York, April 1977; SIAM-AMS Proceedings, Vol. 11, 1977.
22. Yanenko, N. N.: "The Method of Fractional Steps", Springer-Verlag, New York, 1971.

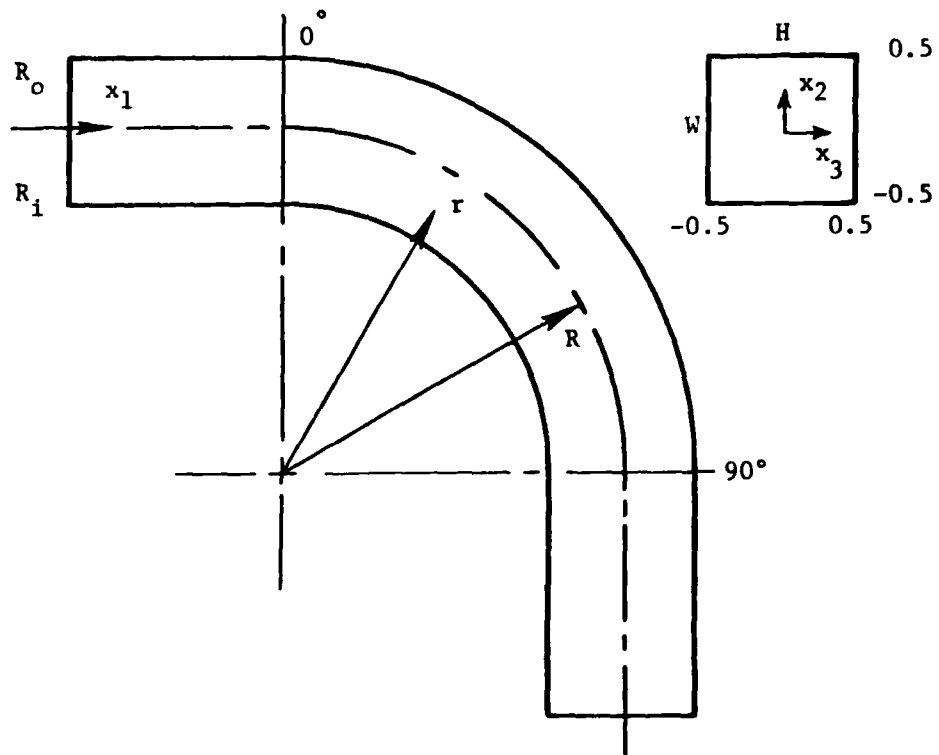


Fig. 1 - Geometry of Square Duct (to scale),
 $R/W = 2.3$, $H/W = 1.0$.

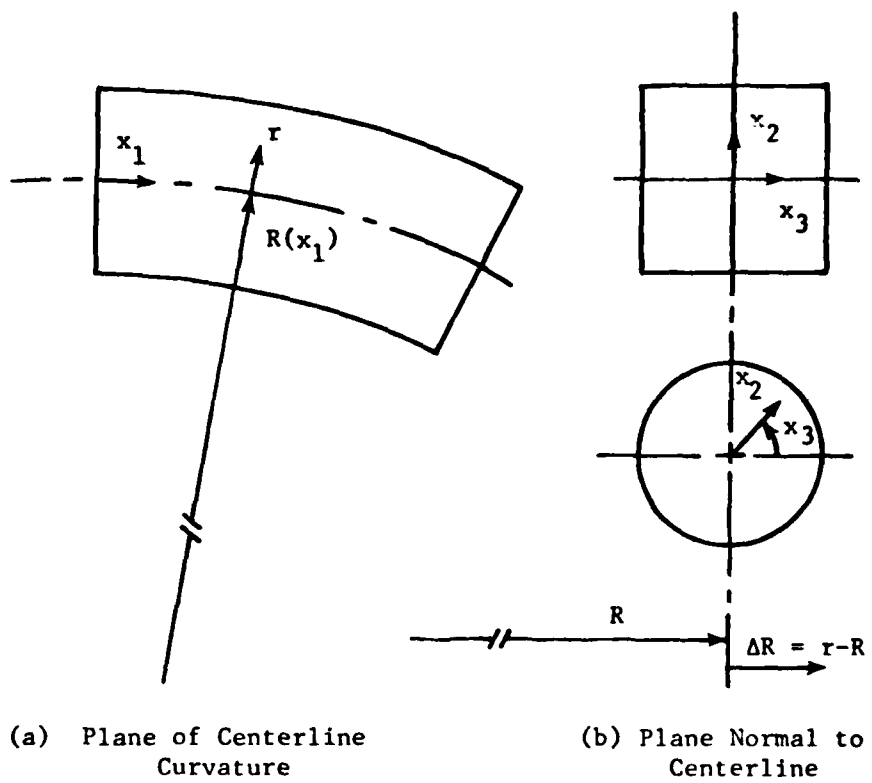


Fig. 2 - Schematic of Coordinate System.

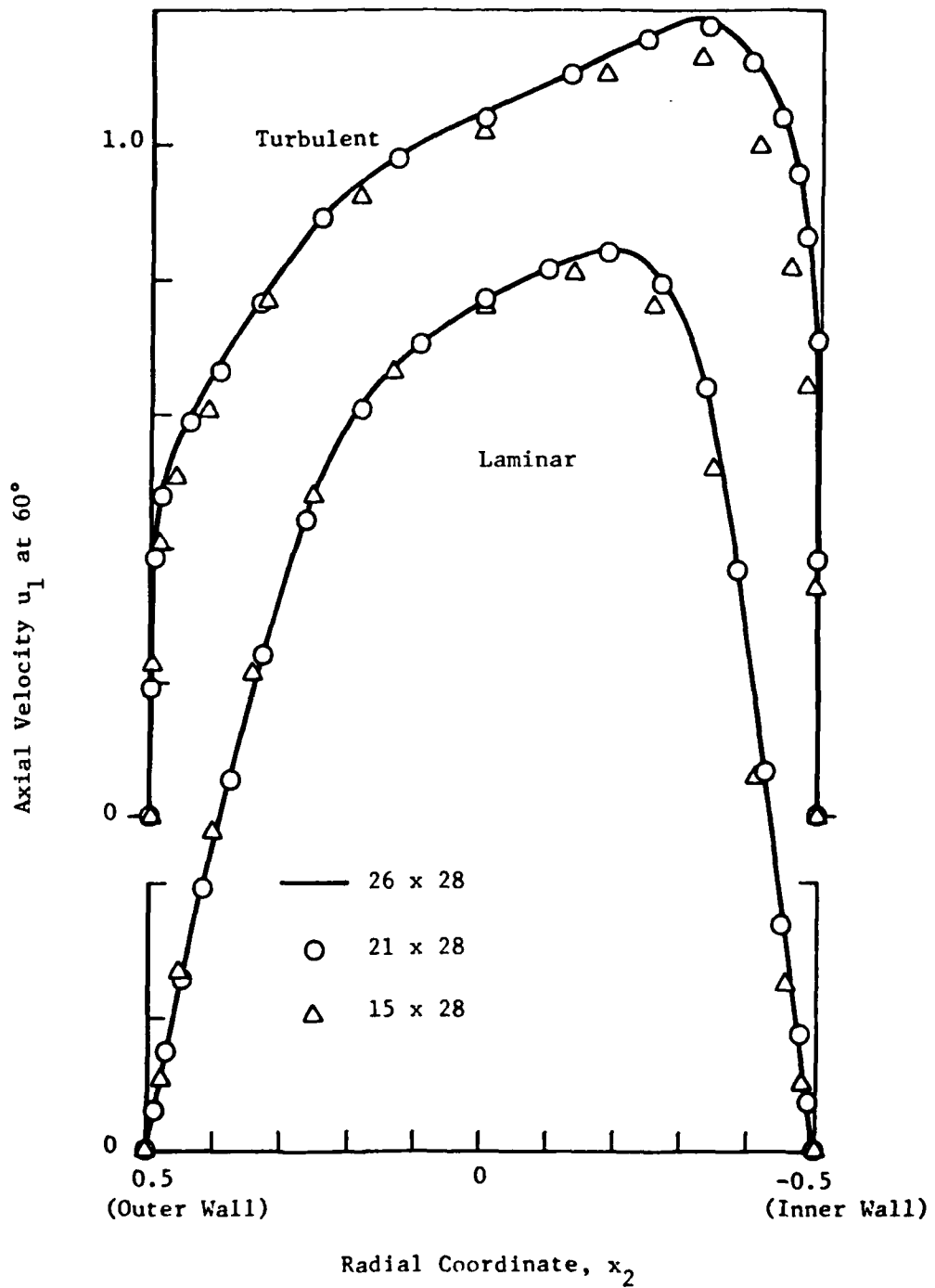


Fig. 3 - Radial Mesh Refinement for Two-Dimensional Channel.

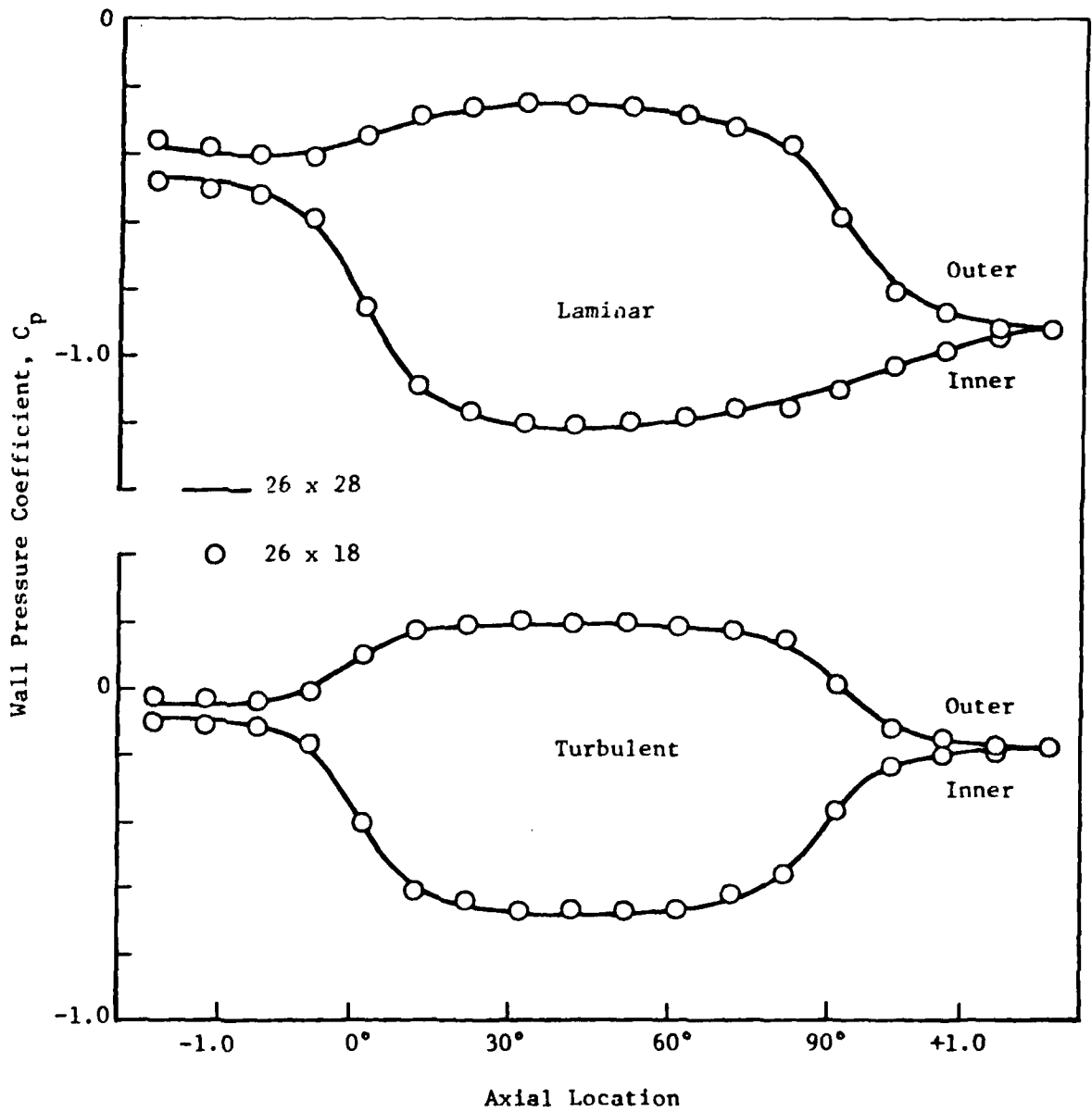


Fig. 4 - Axial Mesh Refinement for Two-Dimensional Channel.

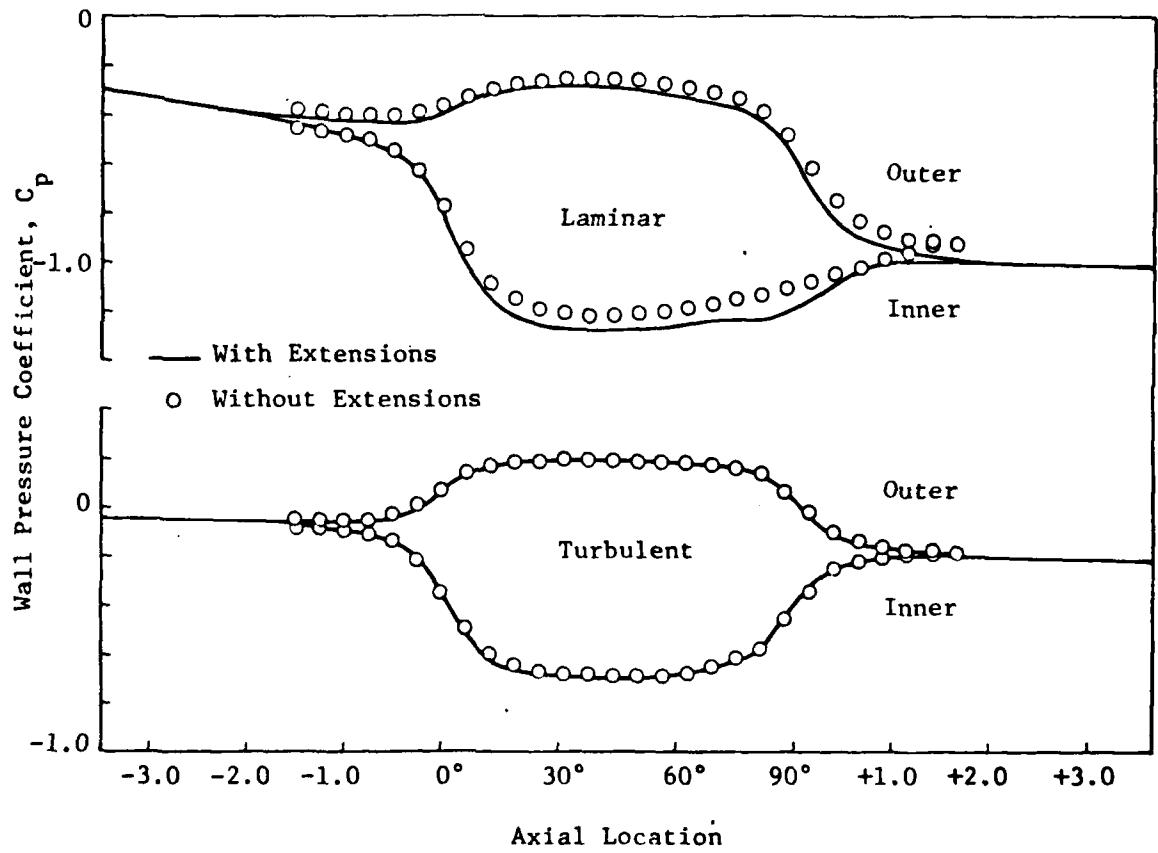


Fig. 5 - Effect of Extending Upstream and Downstream Segments of Two-Dimensional Channel:

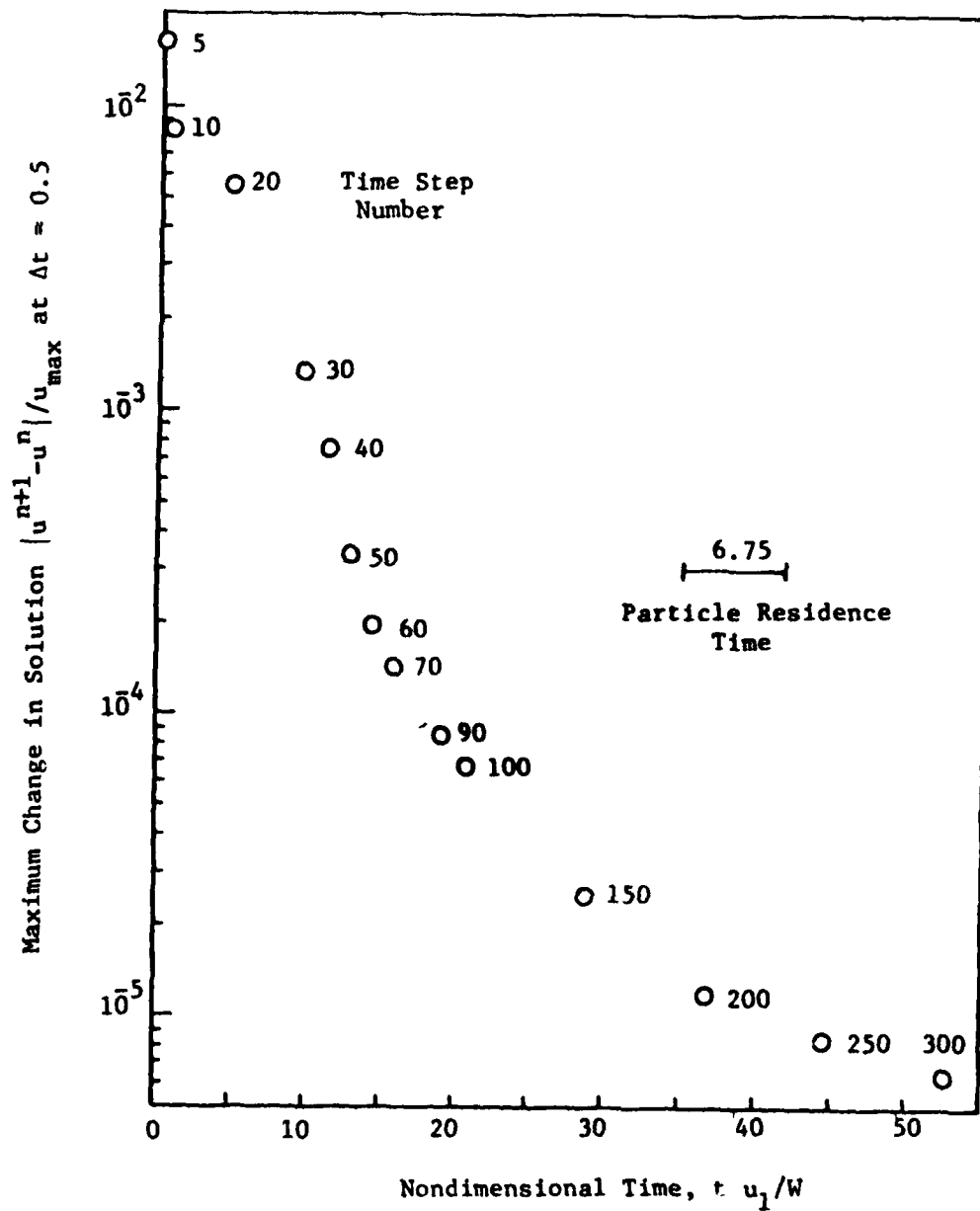


Fig. 6 - Convergence Rate for Two-Dimensional Turbulent Channel Flow.

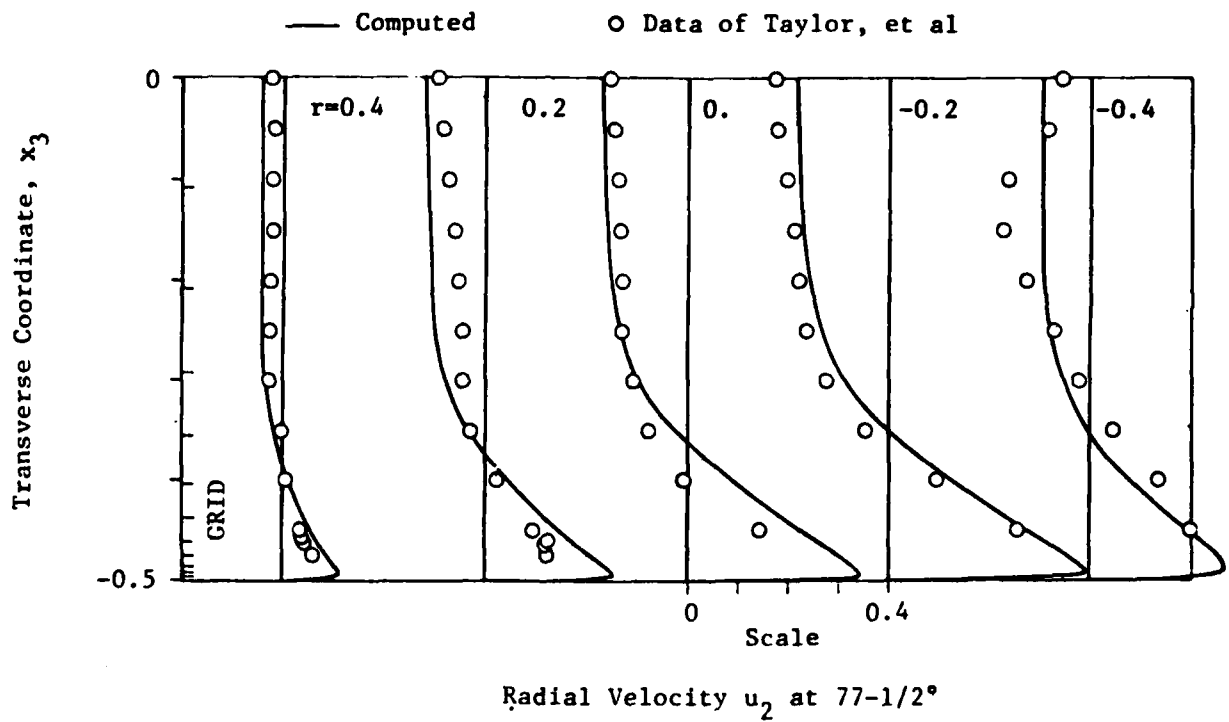


Fig. 8 - Radial Velocity Profiles for Three-Dimensional Turbulent Duct Flow (Inner Wall to Right).

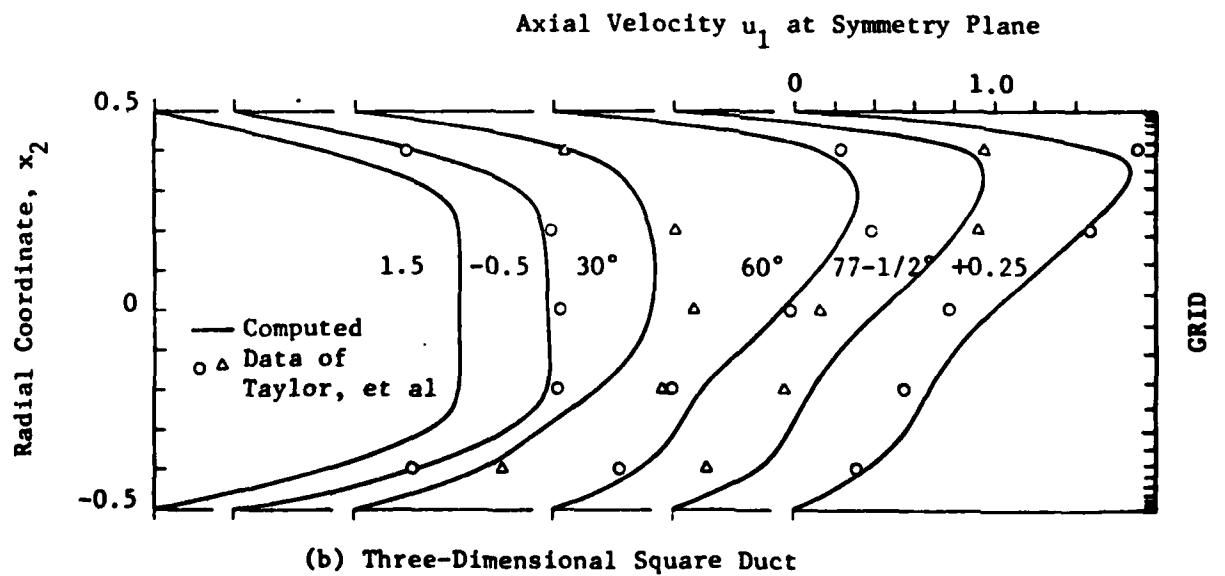
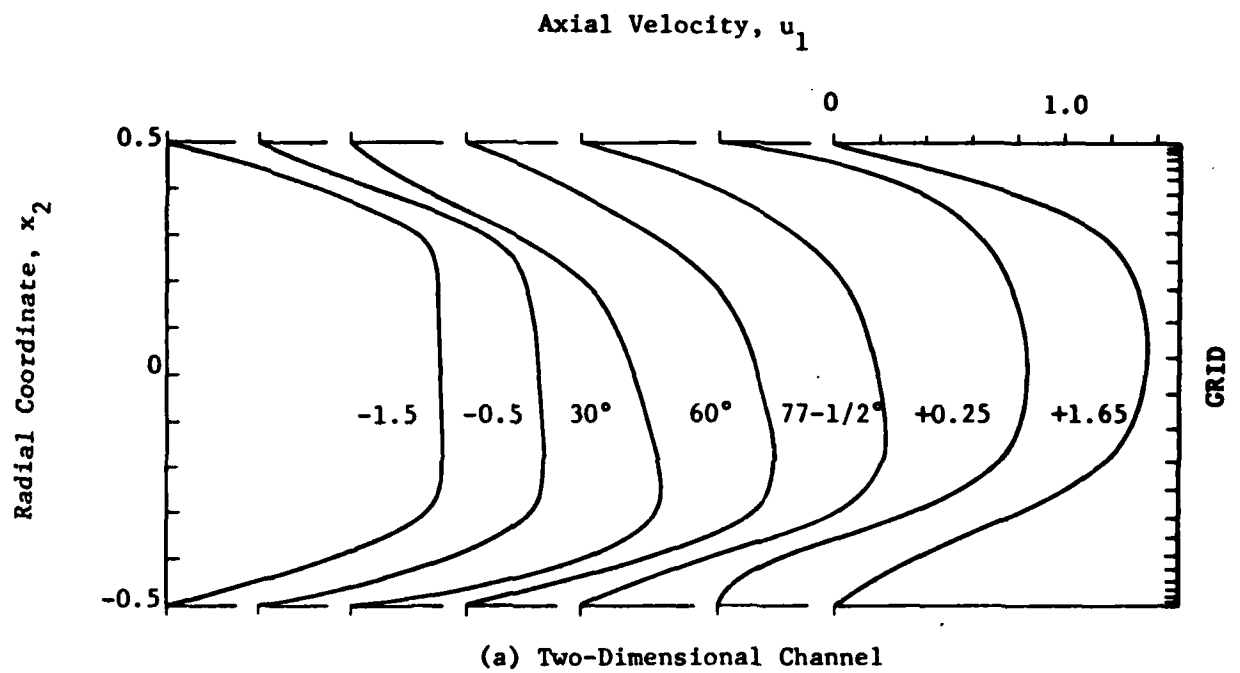


Fig. 9 - Axial Velocity Profiles for Laminar Flow in Two and Three Dimensions (Curves are Labeled by Axial Location; $x_2 = -0.5$ is Inner Wall).

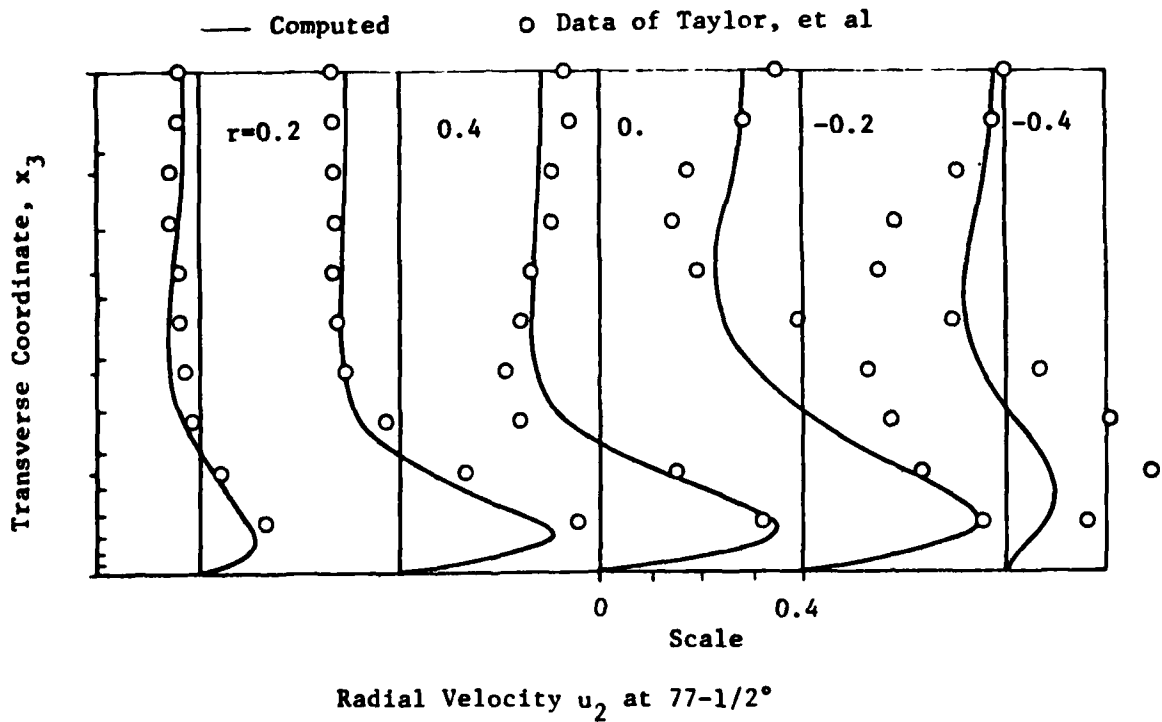


Fig. 10 - Radial Velocity Profiles for Three-Dimensional Laminar Duct Flow (Inner Wall to Right).

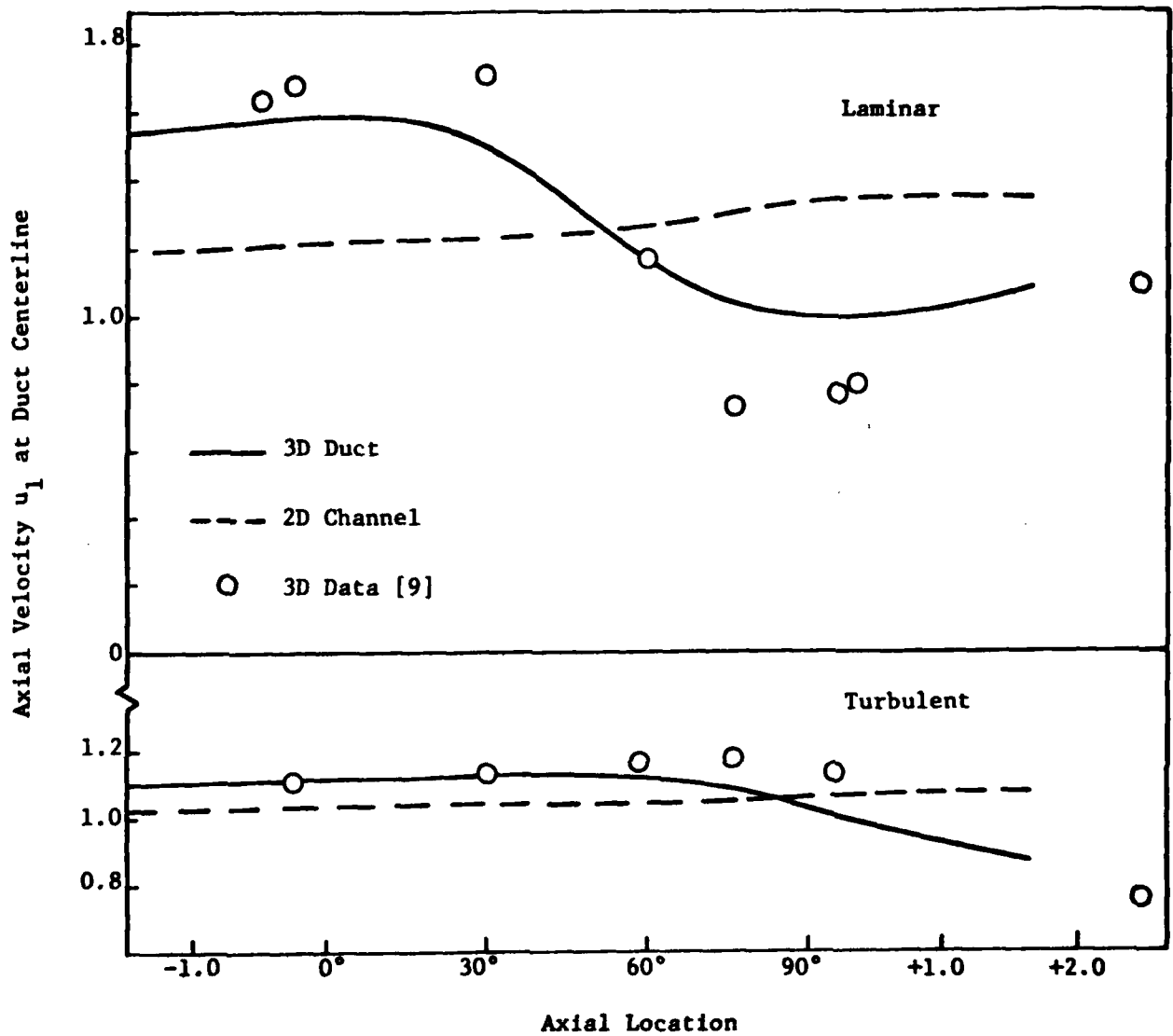


Fig. 11 - Axial Development of Axial Velocity at Duct Centerline.

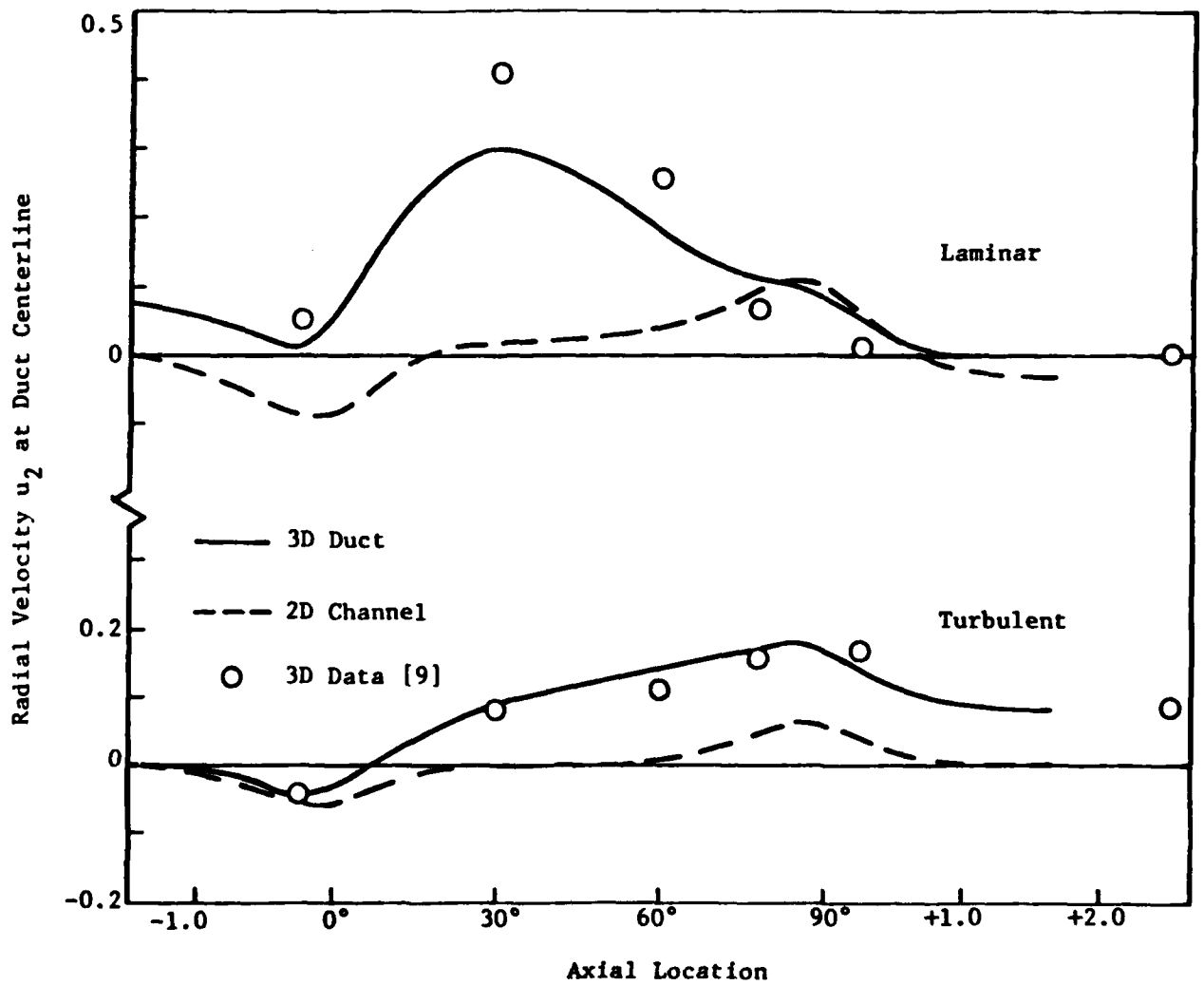


Fig. 12 - Axial Development of Radial Velocity at Duct Centerline.

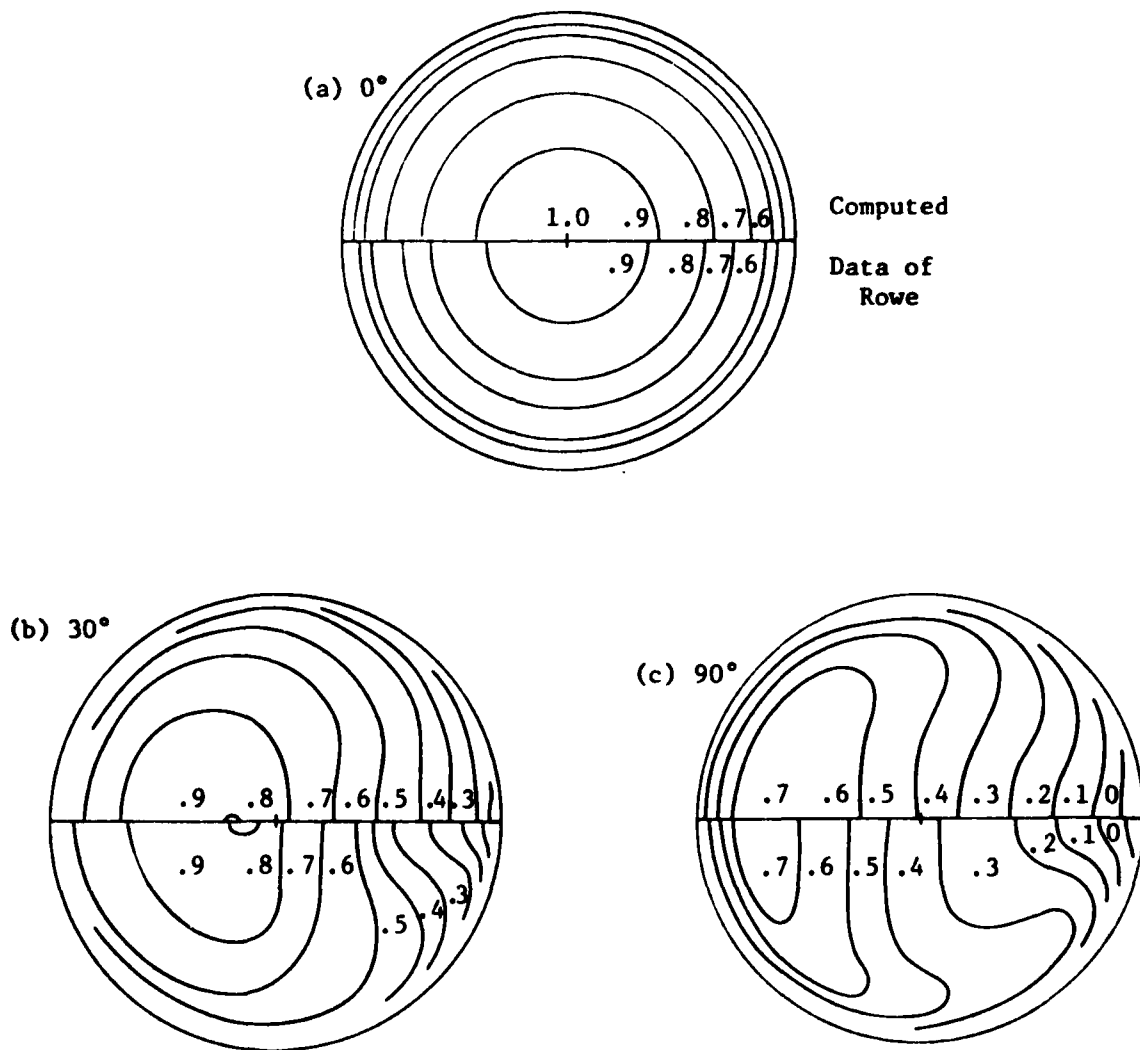


Fig. 13 - Total Pressure Contours for Turbulent Flow
in a Pipe Bend with $Re = 2.36 \times 10^5$, $R/D = 12$
(Inside of Bend is to Right).

ONR DISTRIBUTION LIST FOR UNCLASSIFIED
TECHNICAL REPORTS AND REPRINTS ISSUED UNDER CONTRACT N00014-79-C-0713

All addressees receive one copy unless otherwise specified.

Defense Documentation Center
Cameron Station
Alexandria, VA 22314 12 copies

Professor Bruce Johnson
U.S. Naval Academy
Engineering Department
Annapolis, MD 21402

Library
U.S. Naval Academy
Annapolis, MD 21402

Technical Library
David W. Taylor Naval Ship Research
and Development Center
Annapolis Laboratory
Annapolis, MD 21402

Professor C. -S. Yih
The University of Michigan
Department of Engineering Mechanics
Ann Arbor, MI 48109

Professor T. Francis Ogilvie
The University of Michigan
Department of Naval Architecture
and Marine Engineering
Ann Arbor, MI 48109

Office of Naval Research
Code 211
800 N. Quincy Street
Arlington, VA 22217

Office of Naval Research
Code 438
800 N. Quincy Street
Arlington, VA 22217 3 copies

Office of Naval Research
Code 473
800 N. Quincy Street
Arlington, VA 22217

NASA Scientific and Technical
Information Facility
P. O. Box 8757
Baltimore/Washington International
Airport
Maryland 21240

Professor Paul M. Naghdi
University of California
Department of Mechanical Engineering
Berkeley, CA 94720

Librarian
University of California
Department of Naval Architecture
Berkeley, CA 94720

Professor John V. Wehausen
University of California
Department of Naval Architecture
Berkeley, CA 94720

Library
David W. Taylor Naval Ship Research
and Development Center
Code 522.1
Bethesda, MD 20084

Mr. Justin H. McCarthy, Jr.
David W. Taylor Naval Ship Research
and Development Center
Code 1552
Bethesda, MD 20084

Dr. William B. Morgan
David W. Taylor Naval Ship Research
and Development Center
Code 1540
Bethesda, MD 20084

Director
Office of Naval Research Branch Office
Building 114, Section D
666 Summer Street
Boston, MA 02210

Library
Naval Weapons Center
China Lake, CA 93555

Technical Library
Naval Surface Weapons Center
Dahlgren Laboratory
Dahlgren, VA 22418

Technical Documents Center
Army Mobility Equipment Research Center
Building 315
Fort Belvoir, VA 22060

Technical Library
Webb Institute of Naval Architecture
Glen Cove, NY 11542

Dr. J. P. Breslin
Stevens Institute of Technology
Davidson Laboratory
Castle Point Station
Hoboken, NJ 07030

Professor Louis Landweber
The University of Iowa
Institute of Hydraulic Research
Iowa City, IA 52242

R. E. Gibson Library
The Johns Hopkins University
Applied Physics Laboratory
Johns Hopkins Road
Laurel, MD 20810

Lorenz G. Straub Library
University of Minnesota
St. Anthony Falls Hydraulic Laboratory
Minneapolis, MN 55414

Library
Naval Postgraduate School
Monterey, CA 93940

Technical Library
Naval Underwater Systems Center
Newport, RI 02840

Engineering Societies Library
315 East 47th Street
New York, NY 10017

The Society of Naval Architects and
Marine Engineers
One World Trade Center, Suite 1369
New York, NY 10048

Technical Library
Naval Coastal System Laboratory
Panama City, FL 32401

Professor Theodore Y. Wu
California Institute of Technology
Engineering Science Department
Pasadena, CA 91125

Director
Office of Naval Research Branch Office
1030 E. Green Street
Pasadena, CA 91101

Technical Library
Naval Ship Engineering Center
Philadelphia Division
Philadelphia, PA 19112

Army Research Office
P. O. Box 12211
Research Triangle Park, NC 27709

Editor
Applied Mechanics Review
Southwest Research Institute
8500 Culebra Road
San Antonio, TX 78206

Technical Library
Naval Ocean Systems Center
San Diego, CA 92152

ONR Scientific Liaison Group
American Embassy - Room A-407
APO San Francisco 96503

Librarian
Naval Surface Weapons Center
White Oak Laboratory
Silver Spring, MD 20910

Defense Research and Development Attache
Australian Embassy
1601 Massachusetts Avenue, NW
Washington, DC 20036

Librarian Station 5-2
Coast Guard Headquarters
NASSIF Building
400 Seventh Street, SW
Washington, DC 20591

Library of Congress
Science and Technology Division
Washington, DC 20540

Dr. A. L. Slafkosky
Scientific Advisor
Commandant of the Marine Corps
Code AX
Washington, DC 20380

Maritime Administration
Office of Maritime Technology
14th & E Streets, NW
Washington, DC 20230

Maritime Administration
Division of Naval Architecture
14th & E Streets, NW
Washington, DC 20230

Dr. G. Kulin
National Bureau of Standards
Mechanics Section
Washington, DC 20234

Naval Research Laboratory
Code 2627
Washington, DC 20375 6 copies

Library
Naval Sea Systems Command
Code 09GS
Washington, DC 20362

Mr. Thomas E. Peirce
Naval Sea Systems Command
Code 03512
Washington, DC 20362

Deputy Director
Tactical Technology Office
Defense Advanced Research
Projects Agency
1400 Wilson Boulevard
Arlington, VA 22209

Professor Alexandre J. Chorin
University of California
Center for Pure and Applied
Mathematics
Berkeley, CA 94720

Professor Joseph L. Hammack, Jr.
University of California
Department of Civil Engineering
Berkeley, CA 94720

Professor Paul Lieber
University of California
Department of Mechanical Engineering
Berkeley, CA 94720

Dr. Harvey R. Chaplin, Jr.
David W. Taylor Naval Ship Research
and Development Center
Code 1600
Bethesda, MD 20084

Dr. Francois N. Frenkiel
David W. Taylor Naval Ship Research
and Development Center
Code 1802.2
Bethesda, MD 20084

Mr. Gene H. Gleissner
David W. Taylor Naval Ship Research
and Development Center
Code 1800
Bethesda, MD 20084

Dr. Pao C. Pien
David W. Taylor Naval Ship Research
and Development Center
Code 1521
Bethesda, MD 20084

Professor Francis Noblesse
Massachusetts Institute of Technology
Department of Ocean Engineering
Cambridge, MA 02139

Professor Ronald W. Yeung
Massachusetts Institute of Technology
Department of Ocean Engineering
Cambridge, MA 02139

Professor Allen Plotkin
University of Maryland
Department of Aerospace Engineering
College Park, MD 20742

Professor J. M. Burgers
University of Maryland
Institute of Fluid Dynamics
and Applied Mathematics
College Park, MD 20742

Professor S. I. Pai
University of Maryland
Institute of Fluid Dynamics
and Applied Mathematics
College Park, MD 20742

Computation and Analyses Laboratory
Naval Surface Weapons Center
Dahlgren Laboratory
Dahlgren, VA 22418

Dr. Robert K. -C. Chan
JAYCOR
1401 Camino Del Mar
Del Mar, CA 92014

Dr. Robert H. Kraichnan
Dublin, NH 03444

Mr. Dennis Bushnell
NASA Langley Research Center
Langley Station
Hampton, VA 23365

Technical Library
Naval Ordnance Station
Indian Head, MD 20640

Professor S. F. Shen
Cornell University
Sibley School of Mechanical
and Aerospace Engineering
Ithaca, NY 14853

Professor K. E. Shuler
University of California, San Diego
Department of Chemistry
La Jolla, CA 92093

Dr. E. W. Montroll
Physical Dynamics, Inc.
P. O. Box 556
La Jolla, CA 92038

Mr. Marshall P. Tulin
Hydronautics, Incorporated
7210 Pindell School
Laurel, MD 20810

Dr. J. C. W. Rogers
The Johns Hopkins University
Applied Physics Laboratory
Johns Hopkins Road
Laurel, MD 20810

Dr. Steven A. Orszag
Cambridge Hydrodynamics, Inc.
54 Baskin Road
Lexington, MA 02173

Professor Tuncer Cebeci
California State University
Mechanical Engineering Department
Long Beach, CA 90840

Mr. John L. Hess
Douglas Aircraft Company
3855 Lakewood Boulevard
Long Beach, CA 90801

Dr. C. W. Hirt
University of California
Los Alamos Scientific Laboratory
P. O. Box 1663
Los Alamos, NM 87544

Dr. H. K. Cheng
University of Southern California
University Park
Department of Aerospace Engineering
Los Angeles, CA 90007

Professor J. J. Stoker
New York University
Courant Institute of Mathematical
Sciences
251 Mercer Street
New York, NY 10003

Professor Harry E. Rauch
The Graduate School and University
Center of the City University of
New York
Graduate Center: 33 West 42 Street
New York, NY 10036

Librarian, Aeronautical Laboratory
National Research Council
Montreal Road
Ottawa 7, Canada

Professor H. W. Liepmann
California Institute of Technology
Graduate Aeronautical Laboratories
Pasadena, CA 91125

Professor K. M. Agrawal
Virginia State College
Department of Mathematics
Petersburg, VA 23803

Professor Norman J. Zabusky
University of Pittsburgh
Department of Mathematics
and Statistics
Pittsburgh, PA 15260

Technical Library
Naval Missile Center
Point Mugu, CA 93041

Dr. Harvey Segur
Aeronautical Research Associates
of Princeton, Inc.
50 Washington Road
Princeton, NJ 08540

Professor S. I. Cheng
Princeton University
Department of Aerospace and
Mechanical Sciences
The Engineering Quadrangle
Princeton, NJ 08540

Professor J. T. C. Liu
Brown University
Division of Engineering
Providence, RI 02912

Chief, Document Section
Redstone Scientific Information Center
Army Missile Command
Redstone Arsenal, AL 35809

Mr. J. Enig
Naval Surface Weapons Center
White Oak Laboratory
Room 3-252
Silver Spring, MD 20910

Professor J. F. Thompson
Mississippi State University
Department of Aerophysics and
Aerospace Engineering
State College, MS 39762

AFDRD-AS/M
U.S. Air Force
The Pentagon
Washington, DC 20330

Air Force Office of Scientific
Research/NA
Building 410
Bolling AFB
Washington, DC 20332

Naval Air Systems Command
Code 03
Washington, DC 20361

Naval Air Systems Command
Code 03B
Washington, DC 20361

Naval Air Systems Command
Code 310
Washington, DC 20361

Mr. Raymond F. Sievert
Naval Air Systems Command
Code 320D
Washington, DC 20361

Naval Air Systems Command
Code 5301
Washington, DC 20361

Mr. Robert J. Hansen
Naval Research Laboratory
Code 8441
Washington, DC 20375

Mr. Walter Engle
Naval Sea Systems Command
Code 08
Washington, DC 20362

Dr. Mils Salvesen
David W. Taylor Naval Ship Research
and Development Center
Code 1552
Bethesda, MD 20084

Mrs. Joanna W. Schot
David W. Taylor Naval Ship Research
and Development Center
Code 1843
Bethesda, MD 20084

Dr. George R. Inger
Virginia Polytechnic Institute
and State University
Department of Aerospace and
Ocean Engineering
Blacksburg, VA 24061

Dr. Ali H. Nayfeh
Virginia Polytechnic Institute
and State University
Department of Engineering Mechanics
Blacksburg, VA 24061

Professor C. C. Mei
Massachusetts Institute of Technology
Department of Civil Engineering
Cambridge, MA 02139

Professor David J. Benney
Massachusetts Institute of Technology
Department of Mathematics
Cambridge, MA 02139

Professor E. Mollo-Christensen
Massachusetts Institute of Technology
Department of Meteorology
Room 54-1722
Cambridge, MA 02139

Professor Phillip Mandel
Massachusetts Institute of Technology
Department of Ocean Engineering
Cambridge, MA 02139

Professor J. Nicholas Newman
Massachusetts Institute of Technology
Department of Ocean Engineering
Room 5-324A
Cambridge, MA 02139

Dr. Denny R. S. Ko
Dynamics Technology, Inc.
3838 Carson Street, Suite 110
Torrance, CA 90503

Professor Thomas J. Hanratty
University of Illinois at Urbana-
Champaign
Department of Chemical Engineering
205 Roger Adams Laboratory
Urbana, IL 61801

Air Force Office of Scientific
Research/HA
Building 410
Bolling AFB
Washington, DC 20332

Professor Hsien-Ping Pao
The Catholic University of America
Department of Civil Engineering
Washington, DC 20064

Dr. Phillip S. Klebanoff
National Bureau of Standards
Mechanics Section
Washington, DC 20234

Dr. G. Kulin
National Bureau of Standards
Mechanics Section
Washington, DC 20234

Dr. J. O. Elliot
Naval Research Laboratory
Code 8310
Washington, DC 20375

Mr. R. J. Hansen
Naval Research Laboratory
Code 8441
Washington, DC 20375

Professor A. Roshko
California Institute of Technology
Graduate Aeronautical Laboratories
Pasadena, CA 91125

Dr. Leslie M. Mack
Jet Propulsion Laboratory
California Institute of Technology
Pasadena, CA 91103

Professor Frederick K. Browand
University of Southern California
University Park
Department of Aerospace Engineering
Los Angeles, CA 90007

Professor John Laufer
University of Southern California
University Park
Department of Aerospace Engineering
Los Angeles, CA 90007

Professor T. R. Thomas
Teesside Polytechnic
Department of Mechanical Engineering
Middlesbrough TS1 3BA, England

Dr. Arthur B. Metzner
University of Delaware
Department of Chemical Engineering.
Newark, DE 19711

Professor Harry E. Rauch
The Graduate School and University
Center of the City University of
New York
Graduate Center: 33 West 42 Street
New York, NY 10036

Mr. Norman M. Nilsen
Dyntec Company
5301 Laurel Canyon Blvd., Suite 201
North Hollywood, CA 91607

Professor L. Gary Leal
California Institute of Technology
Division of Chemistry and Chemical
Engineering
Pasadena, CA 91125

Professor Robert E. Falco
Michigan State University
Department of Mechanical Engineering
East Lansing, MI 48824

Professor E. Rune Lindgren
University of Florida
Department of Engineering Sciences
231 Aerospace Engineering Building
Gainesville, FL 32611

Technical Library
Naval Missile Center
Point Mugu, CA 93041

Professor Francis R. Hama
Princeton University
Department of Mechanical and
Aerospace Engineering
Princeton, NJ 08540

Dr. Joseph H. Clarke
Brown University
Division of Engineering
Providence, RI 02912

Professor J. T. C. Liu
Brown University
Division of Engineering
Providence, RI 02912

Chief, Document Section
Redstone Scientific Information Center
Army Missile Command
Redstone Arsenal, AL 35809

Dr. Jack W. Hoyt
Naval Ocean Systems Center
Code 2501
San Diego, CA 92152

Professor Richard L. Pfeffer
Florida State University
Geophysical Fluid Dynamics Institute
Tallahassee, FL 32306

Dr. Gary Chapman
Ames Research Center
Mail Stop 227-4
Moffett Field, CA 94035

Dr. S. Beus
Bettis Atomic Power Laboratory
P.O. Box 79
West Mifflin, PA 15122

Dr. M. Lubert
General Electric Company
Knolls Atomic Power Laboratory
P.O. Box 1072
Schoenectady, NY 12301

Dr. A. K. M. Fazle Hussain
University of Houston
Department of Mechanical Engineering
Houston, TX 77004

Professor John L. Lumley
Cornell University
Sibley School of Mechanical
and Aerospace Engineering
Ithaca, NY 14853

Professor K. E. Shuler
University of California, San Diego
Department of Chemistry
La Jolla, CA 92093

Dr. E. W. Montroll
Physical Dynamics, Inc.
P. O. Box 556
La Jolla, CA 92038

Professor Patrick Leehey
Massachusetts Institute of Technology
Department of Ocean Engineering
Cambridge, MA 02139

Professor Eli Reshotko
Case Western Reserve University
Department of Mechanical and
Aerospace Engineering
Cleveland, OH 44106

Professor P. S. Virk
Massachusetts Institute of Technology
Department of Chemical Engineering
Cambridge, MA 02139

Professor E. Mollo-Christensen
Massachusetts Institute of Technology
Department of Meteorology
Room 54-1722
Cambridge, MA 02139

Professor W. W. Willmarth
The University of Michigan
Department of Aerospace Engineering
Ann Arbor, MI 48109

Office of Naval Research
Code 481
800 N. Quincy Street
Arlington, VA 22217

Professor Richard W. Miksad
The University of Texas at Austin
Department of Civil Engineering
Austin, TX 78712

Professor Stanley Corrsin
The Johns Hopkins University
Department of Mechanics and
Materials Sciences
Baltimore, MD 21218

Mr. M. Keith Ellingsworth
Power Program
Office of Naval Research
800 N. Quincy Street
Arlington, VA 22217

Professor J. A. C. Humphrey
Department of Mechanical Engineering
University of California, Berkeley
Berkeley, CA 94720

Professor Brian Launder
Thermodynamics and Fluid Mechanics Division
University of Manchester
Institute of Science & Technology
P088 Sackville Street
Manchester M601QD, England

Dr. Simion Kuo
Chief, Energy Systems
Energy Research Laboratory
United Technology Research Center
East Hartford, CT 06108